CORA Cork Open Research Archive
Cartlann Taighde Oscailte Chorcaí

Title	The influence of colloidal opal template and substrate type on 3D macroporous single and binary vanadium oxide inverse opal electrodeposition
Authors	O'Hanlon, Sally;McNulty, David;O'Dwyer, Colm
Publication date	2017-01-21
Original Citation	O'Hanlon, S., McNulty, D. and O'Dwyer, C. (2017) 'The Influence of Colloidal Opal Template and Substrate Type on 3D Macroporous Single and Binary Vanadium Oxide Inverse Opal Electrodeposition', Journal of The Electrochemical Society, 164(4), pp. D111-D119. doi:10.1149/2.0121704jes
Type of publication	Article (peer-reviewed)
Link to publisher's version	10.1149/2.0121704jes
Rights	© The Author(s) 2017. Published by ECS. This is an open access article distributed under the terms of the Creative Commons Attribution Non-Commercial No Derivatives 4.0 License (CC BY-NC-ND, http://creativecommons.org/licenses/by-nc-nd/4.0/), which permits non-commercial reuse, distribution, and reproduction in any medium, provided the original work is not changed in any way and is properly cited. For permission for commercial reuse, please email: oa@electrochem.org. [DOI: 10.1149/2.0121704jes] All rights reserved. - https://creativecommons.org/licenses/by-nc-nd/4.0/
Download date	2026-11-16 11:55:31
Item downloaded from	https://hdl.handle.net/10468/3538



University College Cork, Ireland
Coláiste na hOllscoile Corcaigh

The Influence of Colloidal Opal Template and Substrate Type on 3D Macroporous Single and Binary Vanadium Oxide Inverse Opal Electrodeposition

Sally O'Hanlon,[a] David McNulty,[a] and Colm O'Dwyer[a,b,*,z]

[a]*Department of Chemistry, University College Cork, Cork T12 YN60, Ireland*
[b]*Micro-Nano Systems Centre, Tyndall National Institute, Lee Maltings, Cork T12 R5CP, Ireland*

We report on the electrodeposition of 3D macroporous vanadium oxide inverse opals and binary inverse opals on transparent conducting oxide substrates and stainless steel and thermally oxidized stainless steel substrates. The electrodeposition follows a diffusion limited growth mode to form 3D porous crystalline V_2O_5 after removal of a colloid photonic crystal template of self-assembled polystyrene spheres. Inverse opals were grown using spheres ranging in diameter from 0.5 μm to 6 μm, and binary inverse opals were also electrodeposited using binary mixtures of sphere sizes. We demonstrate that the ionic diffusion that leads to growth has charge-to-mass Coulombic efficiency ranging from 60–90%, depending on the voltage used. Additionally, the tortuosity in ionic diffusion through the opal to the substrate is significantly increased when large sphere diameter templates and binary opal templates are used. Analysis of the contribution of true substrate active area and the influence of template structure on ionic diffusivity confirms that inverse opal growth is dictated by the size of opal spheres, interstitial void clogging by smaller spheres in binary opals, and the conductivity of the substrate active area. The crystallinity of the inverse opal is consistent and a function of applied voltage, and attains phase pure orthorhombic V_2O_5.

© The Author(s) 2017. Published by ECS. This is an open access article distributed under the terms of the Creative Commons Attribution Non-Commercial No Derivatives 4.0 License (CC BY-NC-ND, http://creativecommons.org/licenses/by-nc-nd/4.0/), which permits non-commercial reuse, distribution, and reproduction in any medium, provided the original work is not changed in any way and is properly cited. For permission for commercial reuse, please email: oa@electrochem.org. [DOI: 10.1149/2.0121704jes]
All rights reserved.



Manuscript submitted October 17, 2016; revised manuscript received December 22, 2016. Published January 21, 2017.

Inverse opal (IO) structures have found use in a range of applications including catalysis,[1] gas sensing,[2–6] and optical switches,[7] and in numerous optoelectronic and photonic applications[8–12] when fashioned as photonic crystals.[13] Many materials can now be formed into 3D macroporous IO structures[14–17] and recent applications of IOs to electrochemical energy storage has proven that their open-worked structure promotes more stable Li-ion intercalation during cycling.[13,18] IOs are typically formed by infilling a material into the interstitial spaces of a 3D sphere template. Removal of the sphere template allows the formation of interconnected, highly porous structures with pore sizes defined by the initial sacrificial template. Due to their high surface areas, IO structures have exhibited improved rate capability in Li-ion batteries from decreased path lengths for Li^+ insertion[2,19–21] which is crucial for their potential future use in demanding applications such as electric vehicles (EVs) and consumer electronics. Rate limitations associated with standard Li-ion batteries can be improved in principle due to shorter diffusion lengths in the 3D architecture,[22,23] which can be manipulated by altering the pore size in the initial template structure[2] during growth. IOs provide scope for improved performance[24] by enhancing cycle-life due to their ability to withstand repeated lithiation/delithiation.[19,25–27] IOs have also been investigated for use in solar cells[28,29] and electrochromic devices,[22,30,31] which benefit from the large active surface-area to volume ratio and the ability of IOs to be fashioned with porosity that enhances the capture and waveguiding of light at certain energies at various angles of incidence, because IOs exhibit a pseudo photonic bandgap structure.[32]

Vanadium pentoxide (V_2O_5) has been the subject of much research for over 40 years[33] and has been widely investigated as a cathode material for Li-ion batteries due to its high theoretical specific capacity, according to the following intercalation reaction: $V_2O_5 + xLi^+ + xe^- \leftrightarrow Li_xV_2O_5$ ($0 < x < 3$).[34,35] V_2O_5 is useful for reversible Li-ion insertion and removal due to its mixed valance and layered structure.[25,31] The mixed valence (V^{4+} and V^{5+}) of V_2O_5 allows for material expansion during intercalation with more electrolyte accessing the increased surface area, also helping decrease structural deformation of the material.[25,36] To date, a wide range of nanostructured V_2O_5 materials (including nanowires, nanorods, etc.[34,37]) have been examined as Li-ion cathode materials. In particular, 3D V_2O_5 IO structures have shown extremely promising results in both and half-cell and full-cell configurations, prompting further research into mechanism of formation and control over their structure, geometry, crystallinity, size and composition/valence.[38]

V_2O_5 IOs have been formed using various routes including simple dropcast methods and more controlled electrodeposition (ED) approaches.[7,25,32] ED of V_2O_5 IOs has been achieved using a $VOSO_4$ aqueous solution (with subsequent heating allowing a transformation to crystalline V_2O_5) producing dense material in the sphere template voids. Aside from the many alternative infiltration methods, creating binary inverse opals from binary opal templates has received little attention. Control in the position of mixtures of large and small spheres is non-trivial, and infiltration and crystallization protocols often require temperatures and times sufficient to remove large and small polymeric spheres, whose decomposition times are different. Electrodeposition allows for more precisely controlled growth of the V_2O_5 compared to dropcasting approaches. Using ED, IOs can be formed on a wide range of conductive substrates such as steel, FTO/ITO, aluminum etc. along with different materials,[29,39–44] further highlighting the versatility of this approach.[25,45,46] However, very few systematic investigations on the factors influencing IO formation using ED (i.e. impact of sphere template, ED voltage and time, choice of substrate etc.) have been reported.[47,48]

This study provides a detailed investigation into the preparation of V_2O_5 IOs focusing on the use of ED into preformed colloidal opal templates as a function of ED parameters (sphere size, voltage, time and substrate). Initially, the influence of substrate for ED of IO structures is investigated by comparing IO nucleation and growth on stainless steel (SS), heated (oxidized) stainless steel (HSS) and FTO. The influence of ED voltage is also investigated for these substrates, where the most uniform IO formation is found on FTO substrates across the range of voltages examined. The morphology and composition of the IOs is monitored using Raman scattering and electron microscopy. We summarize the relative growth mechanisms of IO materials by ED and compare the influence of diffusion path tortuosity and effective surface area on the growth and the final structure. Finally, we investigate the electrodeposition on binary (two scales of structured porosity) inverse opals of V_2O_5.

*Electrochemical Society Member.
[z]E-mail: c.odwyer@ucc.ie

Downloaded on 2017-01-30 to IP 143.239.102.113 address. Redistribution subject to ECS terms of use (see ecsdl.org/site/terms_use) unless CC License in place (see abstract).

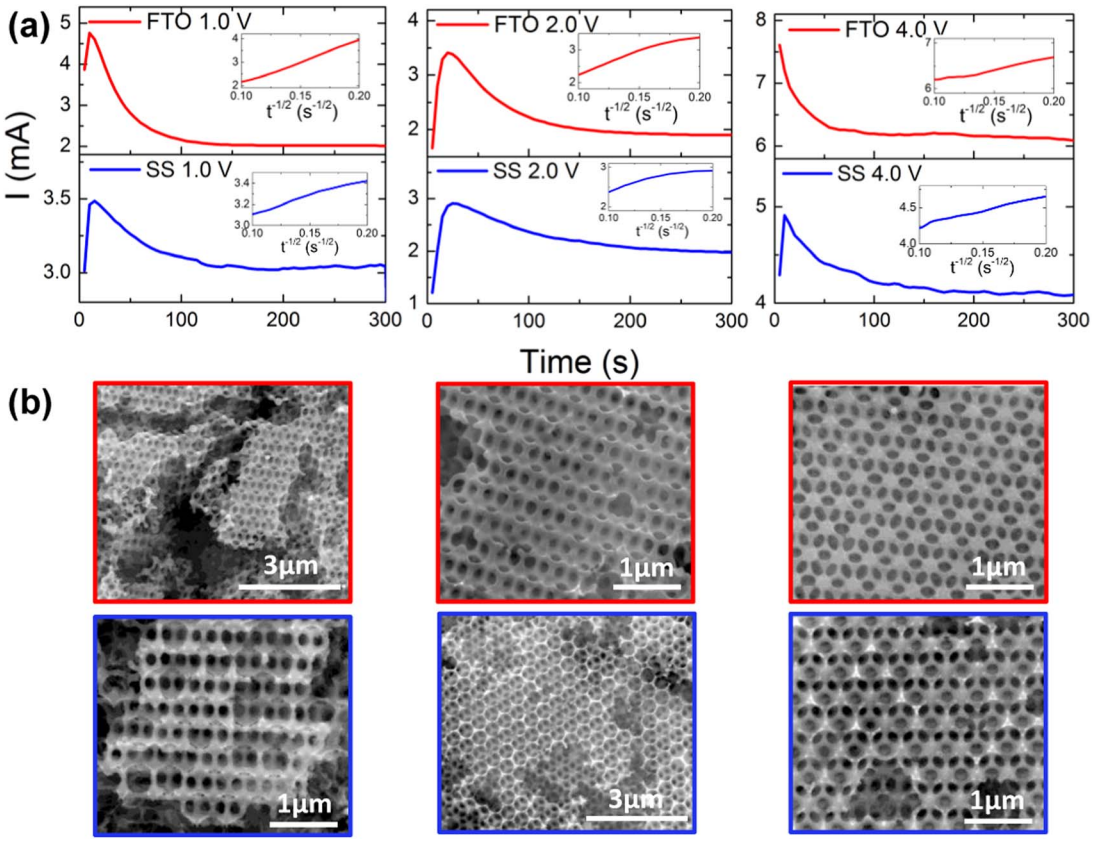


Figure 1. (a) Current (*I*) versus time (*t*) chronoamperograms for IO electrodeposition into a PS sphere template on FTO-coated glass (top panels) and SS (bottom panels) at voltages of 1.0, 2.0 and 4.0 V for 300 s. Current (*I*) versus $t^{-1/2}$ plots for the decreasing portion of the *I* vs *t* transients are shown inset. (b) SEM images for each IOs grown on FTO (top row) and SS (bottom row) at 1.0 V, 2.0 V and 4.0 V for 300 s.

Experimental

Opal template fabrication.—Colloidal crystal templates were formed on conductive substrates of pre-heated stainless steel (SS) foil, SS foil, and FTO coated glass of ∼1 cm × 1 cm geometric area by drop-casting of 0.5 µm diameter polystyrene (PS) spheres. The PS spheres from Polysciences Europe GmbH were functionalized with sulfate groups to aid in self-assembly. Colloidal crystal templates were also formed on ∼1 cm × 1 cm area conductive substrates of pre-heated SS foil and SS foil using 2 µm and 6 µm diameter PS spheres.

Electrodeposition of vanadium oxide.—Vanadium pentoxide was infilled by electrodeposition at room temperature using a VersaSTAT3 Potentiostat. Various potentials from 0.5 V to 4 V were applied versus a saturated calomel (SCE) reference electrode in a three-electrode cell with a platinum mesh as counter electrode and the PS template-coated substrate as the working electrode. The electrolyte was made by adding 2.53 g of $VOSO_4.\chi H_2O$, used as purchased from Sigma Aldrich, to a 1:1 (v/v) mixture of 20 ml of deionized water and 20 ml of ethanol to form a 0.25 M $VOSO_4.\chi H_2O$ solution. After deposition, samples were heated to 300°C for 24 h to remove the spheres, resulting in the formation of a network of crystalline V_2O_5. The electrodeposition of vanadium oxide was performed for PS templates on pre-heated SS foil substrates, SS foil substrates and FTO-coated glass. The mass of SS changes slightly on heating due to oxide formation after heating 300°C, and the mass is re-measured after substrate cooling before opal sphere templates were drop-cast.

Structural and elemental characterization.—Structural and morphological characterization of the electrodeposited IO materials after sphere template removal was performed using a Zeiss Supra 40 SEM at accelerating voltages in the range 5–10 kV. Crystallographic information was investigated using Raman scattering spectroscopy and X-ray diffraction. Raman scattering was acquired using a QE65 PRO Ocean Optics spectrometer with a 50 µm slit width. Excitation was provided by a Laser Quantum GEM DPSS single transverse mode CW green laser emitting at λ = 532 nm. The spectral resolution of the spectrometer ranges from 17.5–10.5 cm^{-1} between 300–4000 cm^{-1}. The laser source was focused onto the sample surface through an objective of 4×, 10×, 20× or 40 × magnifications with numerical apertures (N.A.) of 0.10, 0.25, 0.40 and 0.60, respectively. Spectra were collected under a variety of different laser powers from 10 mW to 100 mW. The laser power densities (LPDs) calculated from these settings range between 15.41 W cm^{-1} for 4× magnification with 10% laser power to 924.3 W cm^{-1} for 40× magnification with 100% laser power. X-ray diffraction was performed on a Philips Xpert PW3719 diffractometer using Cu Kα radiation.

Results and Discussion

Electrodeposition of inverse opal V_2O_5 on stainless steel and FTO.—The electrodeposition (ED) process for inverse opals (IO) produces chronoamperometric current density-time transients that define the growth and nucleation characteristics of the V_2O_5 within the interstitial voids of the parent opal templates.[7,25,32,42] The IO materials were electrodeposited into PS sphere templates on stainless-steel (SS) foil substrates and also on fluorine-doped tin oxide (FTO) coated glass under potentiostatic conditions at a range of voltages, and the respective chronoamperograms are shown in Fig. 1a. In order to compare the influence of applied voltage during ED on the growth of the inverse opal (IO) on these substrates, the samples were electrodeposited at a range of 1.0 V, 2.0 V or 4.0 V for 5 mins. The higher potentials of 2.0 V and 4.0 V are used due to the insulating nature of the polymeric opal tem-

Downloaded on 2017-01-30 to IP 143.239.102.113 address. Redistribution subject to ECS terms of use (see ecsdl.org/site/terms_use) unless CC License in place (see abstract).

plate, the ionic diffusion rate to the surface, and continued ED occurs onto a more resistive V_2O_5 volume after the initial wetting of the electrode surface. From Fig. 1a, the V_2O_5 IOs on FTO electrodeposited at 1.0 V and 2.0 V showed a non-zero initial current associated with instantaneous nucleation, which then gradually decreased once the available FTO surface was covered by V_2O_5, to a steady IO growth at ∼2.0 mA and 1.9 mA, respectively. At 4.0 V on FTO, the current started at ∼7.6 mA which decreased rapidly to a relatively growth at a current of ∼6.0 mA. Electrodeposition onto SS at 1.0 V, 2.0 V and 4.0 V produced similar IO growth patterns to that on FTO, with instantaneous nucleation again which gradually decreases to currents of ∼3.1, 2.0, and 4.1 mA, respectively. V_2O_5 electrodeposited at these various voltages on FTO and on SS provided the characteristic profiles for 3D growth via continuous nucleation, with non-zero current, rapid rise to formation of peak and gradual decay to a steady current. IO electrodeposition is similar for both substrates at 2.0 V and consistently produced higher quality IO structures, defined internal wall structure and is diffusion limited growth which ensures continual growth of V_2O_5 throughout the interstitial voids of the opal template. Negligible current and IO growth is found at redox potentials of V^{4+}/V^{5+} in aqueous solution, where, as Rehnlund[45] discusses, V_2O_5 precipitates from more V^{5+} content formed at higher potentials.

The chronoamperograms in Fig. 1a are also plotted as I versus $t^{-1/2}$ curves, which allowed for the diffusion coefficient to be calculated using the Cottrell equation,[49]

$$I = \frac{nFAD^{1/2}C_0^*}{(\pi t)^{1/2}} \quad [1]$$

where I is the current, n is the number of electrons transferred, F is faraday's constant, A is the area of the electrode, C_0^* is the concentration of the electroactive species, t is the deposition time and D is the diffusion coefficient for the species.[50,51] The diffusion coefficient values were calculated for the opal template-coated FTO substrates at 1.0 V, 2.0 V, 4.0 V to be 7.84×10^{-7}, 6.09×10^{-7}, and 2.60×10^{-7} $cm^2\ s^{-1}$, respectively. The corresponding D values for IO electrodeposition on SS substrates at were 1.50×10^{-7}, 4.10×10^{-7}, and 1.64×10^{-7} $cm^2\ s^{-1}$, respectively.

Shown in Fig. 1b are the corresponding SEM images of the electrodeposited IO morphology. The expected 3D networked and ordered inverse opal material regions are found in all cases. After deposition at 1.0 V, SEM images showed the formation of 3D macroporous structures separated by voids and cracks, which was common on each substrate at this voltage. At 2.0 V, a consistent and well-defined IO is formed, with some large cracks typical of deposition of large areas observable. The V_2O_5 material retains a near-perfect inverse replica of the opal template. Image analysis of the resulting structure (Fig. 2), show that the average IO pore diameter is 460–480 nm after annealing post-ED onto any of the substrate at all of the voltages used, close to the 500 nm of the original PS sphere. The slight reduction stems from the high volume fraction of V_2O_5 formed from ED from VO^{2+} in the intersphere voids. After electrodeposition 4.0 V, SEM images show that the IO structure is clearly formed, but the walls are characteristically thicker. In some cases, slight differences can be seen in SEM micrographs in this case, as SEM micrographs were obtained from the side and top of IO structures. For example, at 90° the (110) face of an IO is seen with a square pore profile, which is different to the hexagonal three-fold seen in plan-view.

The Coulombic (Q/m) efficiency (CE) of the IO electrodeposition on each substrate at all three voltages was also determined from Fig. 1a. In Fig. 3, the cumulative charge passed during ED onto the SS substrate was slightly higher due to its lower resistivity (higher current) than the FTO-coated glass at all voltages. As the ED process was carried out, IO growth within the opal template on FTO and SS substrates showed a linear variation in cumulative charge. The comparison is due to a similar nucleation and growth mechanism (*cf.* Fig. 1a). The total charge passed when electrodeposited at 1.0 V was found to be ∼0.60 C for ED on the FTO substrate and 0.52 C for ED into the template on the SS substrate. At 2.0 V, the total charge passed during

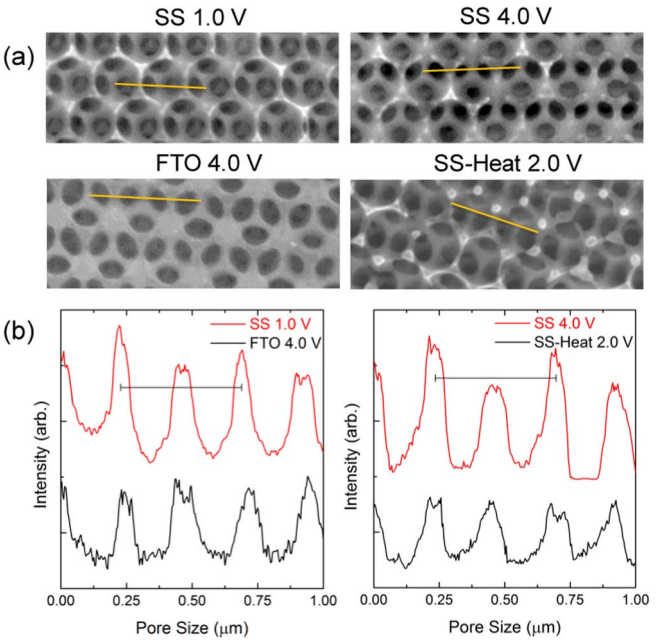


Figure 2. (a) SEM images of electrodeposited and annealed V_2O_5 IOs formed on SS at 1.0 and 4.0 V, on FTO at 4.0 V and on heated SS electrodes at 2.0 V. (b) Linescan profiles acquired from 8-bit grey-scale chennels from SEM images of V_2O_5 IOs in (a).

ED was found to be at ∼0.57 C on FTO and 0.59 C on SS, and at 4.0 V the cumulative charge values were found to be ∼1.83 C on FTO and 4.31 C on SS. The slightly reduced charge passed on FTO corresponds to a lower overall current during the diffusion-limited growth phase. The theoretical electrodeposited mass was also calculated by integration of the total charge passed assuming an $n = 1$ reaction[25] are also plotted in Fig. 3. The mass electrodeposited at 1.0 V on FTO at full Coulombic efficiency is ∼0.28 mg, and for SS the theoretical mass is 0.25 mg. Similarly, the masses for 2.0 V and 4.0 V were found to be ∼0.27 and 0.86 mg on FTO, and ∼0.28 and 2.04 mg on SS, respectively. The samples masses were experimentally measured to be 0.22, 0.25 and 0.57 mg (78.5, 92.6 and 66.3% of full CE) on FTO and 0.23, 0.24 and 1.25 mg (92, 85.7, and 61.3% of full CE) on SS at 1.0 V, 2.0 V, and 4.0 V, respectively. In Fig. 3b, the chronoamperograms are shown at 0.5 V intervals from 1.0 V to 4.0 V on both substrates. These graphs show the gradual increases in current at higher voltages. The characteristic IO growth profile is also found at ∼2.0 V for each substrate and the magnitude of the current peak increases with higher voltage. However, as the voltages increased beyond 3.0 V on the SS substrates, these patterns were replaced with meandering steady current, which also occurred in Fig. 1a at 4.0 V.

To assess the nature of IO electrodeposition on SS compared to FTO, we investigated the influence of thermally oxidized SS on the electrodeposition. The SS substrates were heated at 300°C for 24 h and electrodeposition was carried out under the same parameters as previously investigated in Fig. 1. The heating protocol was investigated as this is often an integral step in material crystallization on metallic electrodes or current electrodes for several applications, particularly batteries, supercapacitors and electrochemical electrodes. Figure 3 shows the chronoamperograms obtained using heated SS (SS-heat) at 1.0 V, 2.0 V and 4.0 V. In Fig. 4a, the chronoamperograms at 2.0 V show the characteristic pattern of growth on SS compared to the corresponding $I(t)$ profiles of growth on SS-heat. This $I(t)$ profile shows a slight increase in current over the 300 s deposition time and remains relatively constant. This $I(t)$ profile is also observed in Fig. 4b on SS-heat, but with different current values. The currents change from ∼0.1 mA at 1.0 V to 3.6 mA at 2.0 V to a very high value of 21 mA at 4.0 V, but with an overall increase as voltage is increased nonetheless. These

Downloaded on 2017-01-30 to IP 143.239.102.113 address. Redistribution subject to ECS terms of use (see ecsdl.org/site/terms_use) unless CC License in place (see abstract).

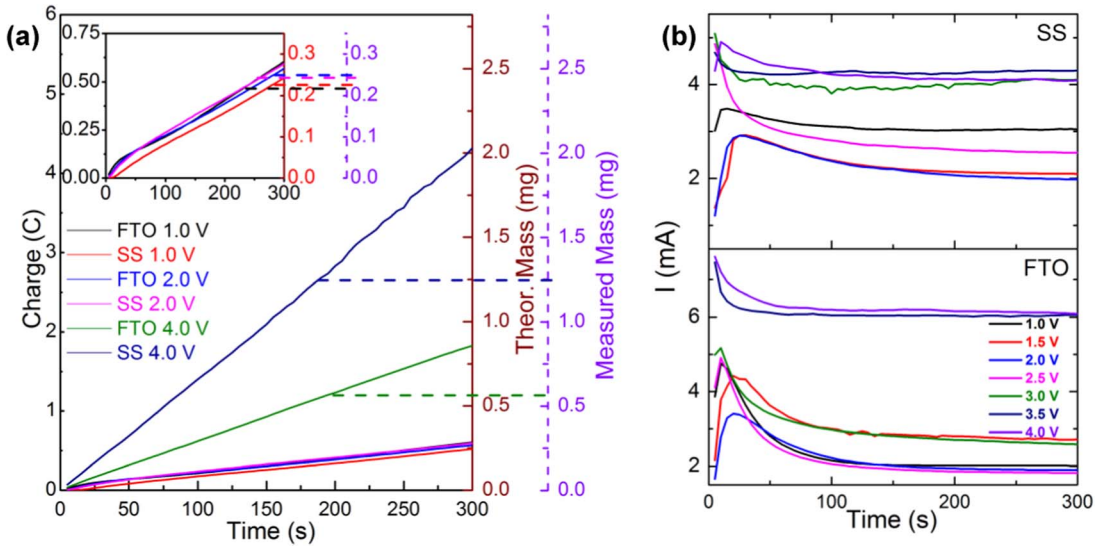


Figure 3. (a) Cumulative charge passed during electrodeposition of V_2O_5 IO on SS and FTO substrates from integration of the potentiostatic $I(t)$ curves at 1.0 V, 2.0 V and 4.0 V for 5 mins. The theoretical mass at full CE according to Faraday's law is indicated in each case. (b) Current (I) versus time (t) chronoamperograms for IO electrodeposition into a PS sphere template on SS (top panel) and FTO-coated (bottom panel) at interval voltages from 1.0 to 4.0 V for 300 s.

$I(t)$ profiles also confirm the presence and effect of the oxide grown on the SS-heat substrate. In spite of a blocking oxide that reduced the magnitude of the current and prevents a non-zero instantaneous rate of nucleation/growth upon polarization, the corresponding SEM images at each voltage shown in Figs. 4a and 4b confirm that high quality 3D structured inverse opal structures are formed on oxidized SS substrates, as we have shown for 1.0, 2.0, and 4.0 V earlier. We also measured the roughness of each substrate type and found that the values are insufficiently high to perturb the positions of spheres to influence the 2D and 3D stracking ordering of the opal, even for the 500 nm spheres. The natural defects that form upon drying after many forms of opal deposition are greater and more numerous than perturbations caused by roughness that are 4–5 orders of magnitude smaller in size (between 0.5–3 nm rms) for our substrates. We have previously investigated the effect of repulsive assembly of the opal template on surfaces with nominal roughness that is similar and as a function of the hydrophobicity and hydrophilicity[52] and it was found that the surface roughness of this magnitude is not a dominant factor for assembly.

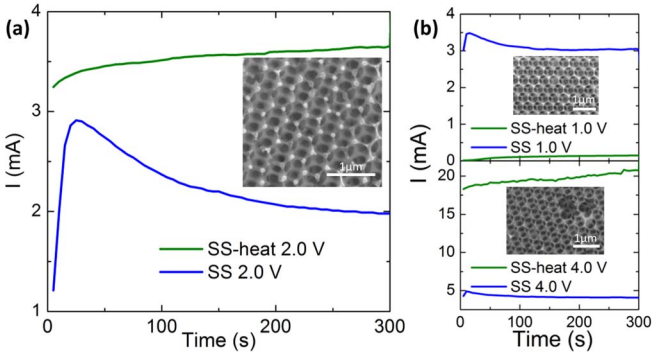


Figure 4. (a) Current (I) vs time (t) obtained during electrodeposition of V_2O_5 IO at a constant voltage of 2.0 V on SS and heated steel substrates. (b) Current (I) vs time (t) obtained during electrodeposition of V_2O_5 IO at a constant voltage of 1.0 V (top) and 4.0 V (bottom) on SS and heated steel substrates. Representative SEM images of the resulting IO structures are shown inset in each case.

Effect of sphere size and binary opal templates on inverse opal electrodeposition.—The effect of sphere size in the colloidal opal template[53–56] on the electrodeposition was also investigated as part of this study. In addition to the 0.5 μm diameter PS spheres, we investigated the influence of ordered colloidal photonic crystal templates using 2 and 6 μm PS spheres over a nominally identical substrate area, on the electrodeposition of V_2O_5 IOs. Figure 5 shows the $I(t)$ responses for V_2O_5 electrodeposited into opal templates using 0.5, 2 and 6 μm diameter PS spheres on heated SS compared to SS for 5 mins at 2.0 V. We observe a common $I(t)$ profile for ED on heated SS (Fig. 5a) and similarly, a consistent $I(t)$ profile for V_2O_5 ED into each template on SS (Fig. 5b). In Fig. 5a, ED into template of different sizes on oxidized SS follows a similar mechanism with currents ranging only from 3 to ~4.5 mA. In Fig. 5b we observed that the magnitude of current ranged from 2 to 5 mA, with the 2 and 6 μm diameter PS spheres having very similar IO growth profiles and currents. A slight increase in the diffusion-limited current transient during potentiostatic ED on oxidized SS-heat is noted using an opal template with larger sphere sizes. Thus, at constant voltage the conductivity of the substrate, the available surface area and tortuosity of the ordered opal template, and as a consequence, the thickness of the opal deposit all influence the rate of ED. The initial surface condition (oxidized or not) has a significant influence on the mechanism of the ED initiation as discussed previously. However, high quality IOs with pore sizes nominally of 500 nm to 6 μm can be electrodeposited.

The effect of sphere size combinations was also investigated. Binary colloidal opal templates were formed and subsequently, IOs were electrodeposited to characterize the nature of binary IO electrodeposition for the first time. Figure 6a shows the chronoamperograms for ED into binary opals comprising 0.5 μm and 2 μm PS spheres, and the mixture of 0.5 μm with 6 μm PS. The $I(t)$ profiles of electrodeposition using 2 μm PS under identical conditions, and separately, 6 μm sphere templated again under identical conditions are overlaid for comparison to the binary IO ED. In each case, the binary IO growth follow similar growth profiles that, after an initial diffusion-limited decrease in current, range from ~3.8 mA to ~4.7 mA as constant ED. The single 2 μm PS current is consistently slightly higher compared to a binary composite including 0.5 μm spheres (from ~5.1 mA to 4.0 mA), while the single 6 μm PS $I(t)$ profile has a slightly lower current compared to a binary colloidal template that includes 2 μm spheres. The corresponding SEM figures are shown in Fig. 6b. While the addition of smaller spheres to an ordered initial binary template does not alter the mechanism of electrodeposition, as evident from

Downloaded on 2017-01-30 to IP 143.239.102.113 address. Redistribution subject to ECS terms of use (see ecsdl.org/site/terms_use) unless CC License in place (see abstract).

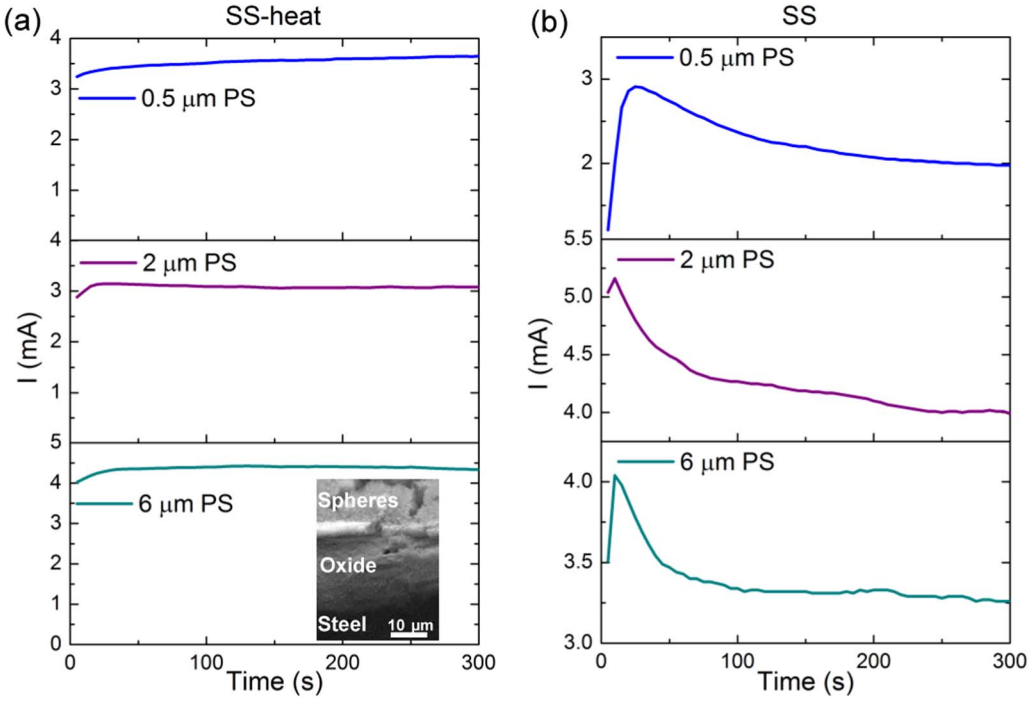


Figure 5. Potentiostatic chronoamperograms for V_2O_5 IO ED into opal templates with sphere sizes of 0.5, 2 and 6 μm at 2.0 V on (a) heated SS and (b) non-heated steel. The cross-sectional SEM image inset in (a) shows the presence of the oxide between the spheres and the SS substrate from preheating.

the shape of the $I(t)$ transients, the resulting structures are much more deformed, and the V_2O_5 is found to be electrodeposited across the surface of the larger spheres creating hollow sphere structures. In mixed deposited using 6 μm spheres, the small sphere structures mask ED over the surface of the larger spheres. Characteristically, small sphere sizes promote interstitial ED; larger sphere sizes tend to form hollow spheres of oxide as they provide significant open surface either side of interstitial voids to form V_2O_5. The diffusion limited Cottrell-form growth transients (I vs $t^{-1/2}$) as employed for single sphere size IO ED in Fig. 1, resulted in D values of 1.9×10^7 and 1.4×10^7 cm^2 s^{-1} for electrodeposition into 0.5 μm + 2 μm and 0.5 μm + 6 μm binary sphere templates, respectively.

Template tortuosity in 3D and active surface influence on inverse opal electrodeposition.—In the hexagonally packed (111) face of the colloidal opal template, there exists trigonal, tetrahedral and octahedral voids that permeate through the first three layers of spheres for example (e.g. Fig. 7). The volume of these interstitial voids is well known to be a function of the sphere size in a similarly ordered opal template. When species diffuse into ordered porous systems, the mechanism of transport has been well established for gaseous infiltration,

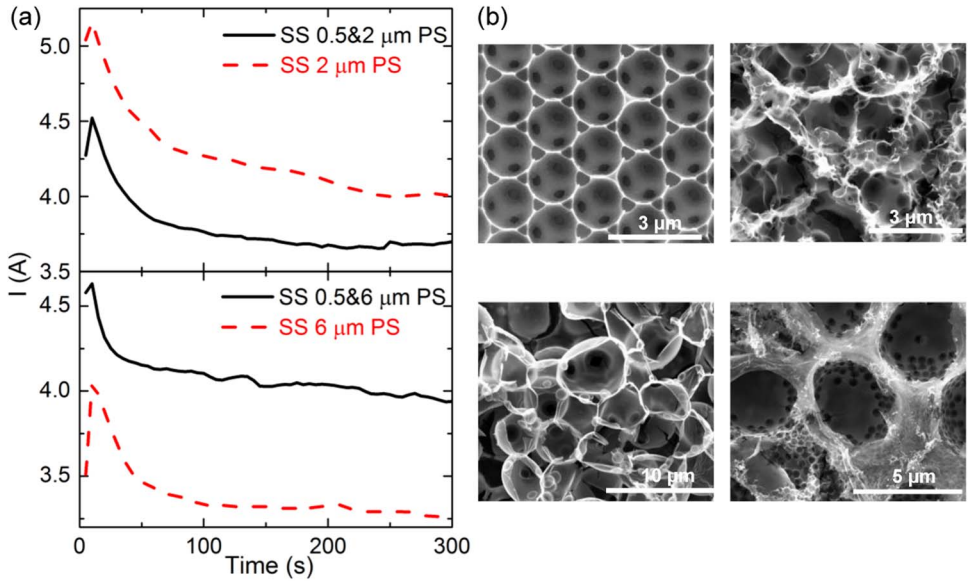


Figure 6. (a) Potentiostatic chronoamperograms for V_2O_5 IO ED into opal templates with sphere size mixtures of 0.5 & 2 μm, and 0.5 & 6 μm against the previous single sphere size templates of 2 μm and 6 μm. (b) SEM images with the single sphere size templates on the left and mixture of spheres on the right, 2 μm on top and 6 μm below.

Downloaded on 2017-01-30 to IP 143.239.102.113 address. Redistribution subject to ECS terms of use (see ecsdl.org/site/terms_use) unless CC License in place (see abstract).

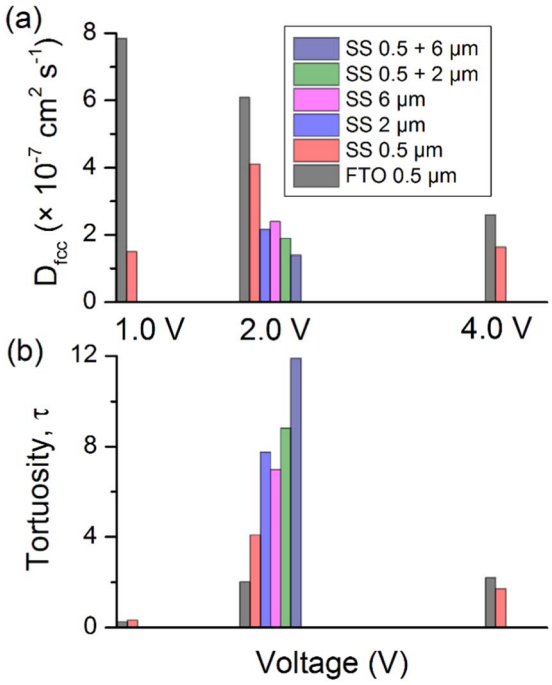


Figure 7. (a) Diffusion constant of VO^{2+} ions to the available surface area on the substrate covered in electrolyte-soaked templates of single sphere and binary sphere sizes, following potentiostatic ED at 1.0, 2.0 and 4.0 V onto SS and FTO. (b) Tortuosity estimates determined using separately acquired diffusion constant values for ED onto uncoated SS and FTO substrates, D_{soln} following Eq. 2.

molecular diffusion liquid wetting, heat conduction, etc.,[57–60] but not for electrodeposition of inverse opals.

The rate of electrodeposition is a function of the available internal volume of the interstitial voids (~26% for full packing, i.e. $V_f = 0.26$), compared to planar electrodeposition on a nominally similar substrate area, and the nature of the single or binary opal template will define the surface area and volume under the first layer of spheres, and thus the subsequent growth. D values were estimated from potentiostatic $I(t)$ profiles in the framework of the Cottrell relation for all IOs formed at 1.0, 2.0 and 4.0 V on FTO and SS substrates, and for binary IOs using mixtures of sphere sizes. Corresponding D values were also acquired from ED onto template-free surfaces of FTO and SS, giving values of 4.75×10^{-6} and 6.45×10^{-6} cm^2 s^{-1}, respectively, to provide D_{soln} values at 2.0 V for both substrates.

The diffusion constant through the opal template, D_{fcc} is proportional to the diffusion coefficient of the VO^{2+} species, D_{soln}, according to

$$\tau = V_f \frac{D_{soln}}{D_{fcc}}, \quad [2]$$

where τ is the tortuosity of the diffusional path of ions through the opal template's 3D porosity.[25,61] The tortuosity in opals was previously examined experimentally and also from computational analysis and shown to be nearly negligible in thick inverse opals already soaked in electrolyte, formed using 350 nm spheres onto a heated-SS substrate. Figure 7a shows the D_{fcc} values determined in the framework of the Cottrell relation under potentiostatic conditions, where the current indicates the resulting reduction and V_2O_5 growth rate. The Coulombic efficiency conversion to mass of IO was shown in Fig. 3. We observe that diffusion of ions within opal templates is fastest for opals on FTO, decreasing at higher voltages. Diffusion onto SS is relatively similar in magnitude, but we note that ionic diffusion to the substrate is retarded somewhat when larger sphere sizes and binary opal templates are used. To examine the influence of tortuosity of ionic diffusional movement, Fig. 7b shows that tortuosity is negligible for 0.5 μm spheres on FTO or SS at 1.0 and 4.0 V, yet is marginally higher at 2.0 V, as the D_{soln} values at 2.0 V on SS were greater than for FTO, due to the difference in electronic conductivity of the substrate (earlier, the oxide exacerbated this effect, removing the instantaneous increase in current upon initial polarization compared to FTO or unheated SS). Opal templates using larger spheres and also binary opal templates (where the small spheres fill the interstitial gaps of the larger colloid), significantly increased tortuous diffusion movement occurs in an already soaked template. There are two primary reasons we propose to account for this observation based on experimental evidence that has not been addressed in computational simulations of tortuous diffusional movement through opals. The first is the interaction of the ions with the surfaces of the template. While the volume of a unit cell remains constant irrespective of the sphere size, the surface area per layer of spheres in the template for V_2O_5 formation is markedly greater for larger spheres.

In Fig. 6, hollows sphere structures are commonly formed from ED into templates with larger spheres. This does not occur with sphere templates in this work of 2 μm diameter or smaller. Secondly, the available volume under the first layer of spheres at the substrate surface (analyzed in more detail below) is nominally identical for any unit cell of spheres, but binary opals provide clogging paths and increase tortuosity when templated as binary opals with larger spheres - smaller spheres tend to fill interstitial voids in binary opals. To correlate the ED mechanism to the measured $I(t)$ response and profile, we estimated the effective initial surface area for each template. The initial nucleation of the IO, for any 2D or 3D growth process via electrodeposition, is a function of the available surface area of the substrate (SS or FTO) and whether or not it has a passive coating or oxide. In this work, we will examine how the sphere size in fcc packing, dictates the available void volume and thus available surface area.

The schematic in Fig. 8a compares the relative number of 0.5, 2 and 6 μm diameter spheres on a surface of equal dimension in relative scale. Nucleation at this surface is the beginning of the infilling of the opal template to create the inverse opal replica and it is immediately clear that the number of available voids is greater for smaller spheres. The available open area between the spheres in the layer touching the substrate is also shown in plane view (Fig. 8b) - we assume that the entire opal is already infilled with electrolyte prior to nucleation of V_2O_5 at the surface. The subsequent growth in all three cases is progressive electrodeposition throughout the 3D distributed voids that is marginally affected by tortuosity for small spheres, but increases for single opal of larger diameter (and correspondingly, thickness). Binary opals have the highest tortuosity effect on ED growth of IOs.

For the 3D opal colloidal template, each unit cell has $\frac{\pi}{3\sqrt{2}}$ packing factor, leaving ~26% free volume in 3D.[62] However for each sphere size, the unit cell parameter is a function of the sphere diameter. In order to rescale this definition to a predefined substrate area and thus number of spheres of each size, we determined the void factor, 1 - P, where P is the packing factor as a volume fraction occupied by the layer of spheres touching the substrate with respect to the total volume of a unit cell with height equal to the diameter of a single sphere (see Fig. 8b), given by

$$1 - P = \frac{\pi}{3\sqrt{3}} \left(\frac{\phi}{\Lambda} \right)^2 \quad [3]$$

where ϕ is the sphere diameter and Λ is the packing parameter or lattice ($\Lambda = \phi$) for the hexagonally close-packed (111) face of the fcc structure.

This provides the total void volume for a single layer of spheres. The corresponding volume at the substrate is then

$$V_{ED} = \frac{1 - P}{2} \quad [4]$$

On a defined substrate nominal dimension, the number of spheres close packed is defined by the sphere size, and thus the total surface

Downloaded on 2017-01-30 to IP 143.239.102.113 address. Redistribution subject to ECS terms of use (see ecsdl.org/site/terms_use) unless CC License in place (see abstract).

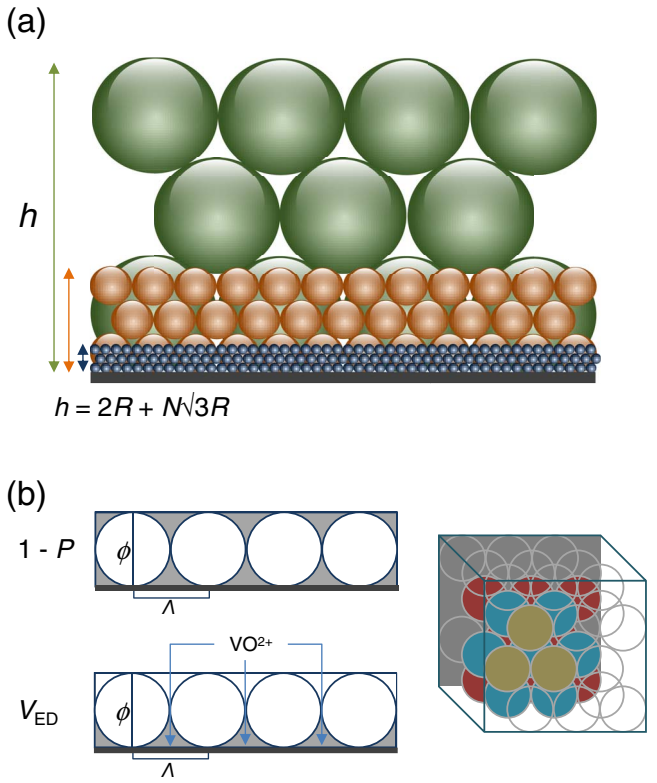


Figure 8. (a) Schematic representation of the first layer of spheres at maximum fcc packing on a surface. (b) Schematic of the first layer of sphere for any fcc opal template. ϕ here represents the sphere diameter, *P* is the packing factor, and Λ is the packing parameter or lattice constant of the sphere assembly. V_{ED} and its represented shaded region indicated the volume for the initial nucleation layer during electrodeposition. The schematic cube shows the octahedral and tetragonal voids that form in a hexagonally packed *abcabc* fcc arrangement of spheres through which VO^{2+} ions diffuse.

area for nucleation under the first layer of spheres is

$$A_{ED} = \frac{V_{ED}}{L_{x,y}}, \qquad [5]$$

where $L_{x,y} = n\Lambda$ for *n* spheres. While the lattice parameter along one side length is $L_y = n\sqrt{2}\phi$ and orthogonal to this, $L_x = n\phi$, we will assume the distance parameter is $\Lambda = \frac{L_{x,y}}{n} = \frac{\phi}{n}$, as the observation of vacancies in sphere coverage or domains of ordered regions typical of opal templates will vary the surface area coverage within this discrepancy.

For 0.5, 2 and 6 μm diameter spheres on 1 cm × 1 cm electrodes, the effective open areas for electrodeposition are all $\frac{\pi}{6\sqrt{3}} \sim 0.302\ cm^2$, and it is general to any sphere size with (111) hexagonally close packed fcc structure on a flat surface. Thus, in a fully soaked template, the available surface area and applied voltage dominate the nucleation mechanism, and the current values on the *I*(*t*) profiles scale with this area. The non-zero instantaneous current values on conductive substrates are influenced by the available open area on a given substrate area and thus the sphere size. The tortuosity, however, is significantly increased when mixtures of spheres are used, especially when large spheres are infilled with small spheres as a binary opal template. But as the experimental and analytical data shows, this binary mixture has the effect of reducing the effective surface area at the substrate, in addition to creating a tortuous path for ionic diffusion (D_{fcc} values are very similar in magnitude). As such, the interaction of ions with large sphere surfaces and tortuosity caused by interstitial infilling with smaller spheres, and reduction in surface area affect the diffusion-limited growth of the resulting IO.

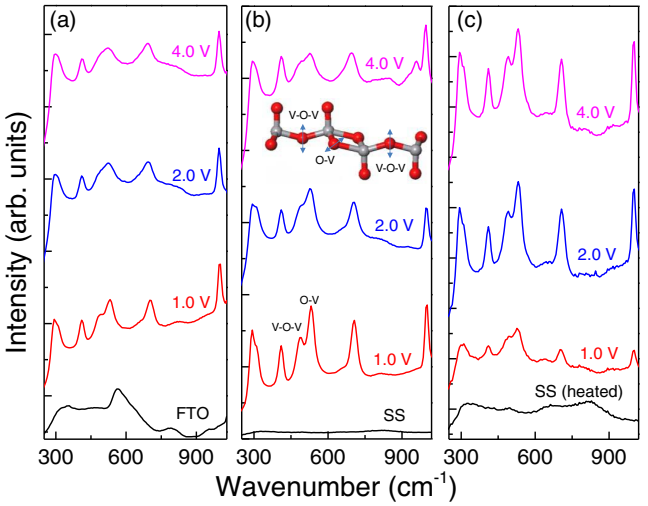


Figure 9. Raman scattering spectra acquired for each substrate and V_2O_5 IO electrodeposited at 1.0 V, 2.0 V, and 4.0 V on (a) FTO, (b) SS, and (c) heated SS substrates.

Crystallinity and phase of electrodeposited V_2O_5 inverse opals.— As the surface oxidation states of SS, the applied voltage, sphere size, thickness and tortuosity of the opal template affect the rate (current) of ED, the morphology of the internal structure of the IO and the mechanism of ED, we used Raman scattering spectroscopy of the optical branch of phonon modes to sensitively determine and compare the crystal structure of the IO in each case. The Raman scattering spectra are shown in Fig. 9, and each substrate's Raman spectrum was also acquired before electrodeposition as a baseline. For the orthorhombic phase of V_2O_5 with a space group P*mmn* and D_{2h} point symmetry, the Raman spectra are now well-established.[63,64] Specifically, to compare the ED crystal structures, we refer to the known Raman active modes for the P*mmn* space group that are modified compared to bulk V_2O_5 because of the crystallization of the electrodeposited IO structured V_2O_5.[65–68] The Raman data for IO ED on FTO-coated glass and the SS substrate showed near identical crystal structure - all dominant modes are observed. In each case, the sharpest peak at the 993 and 997 cm^{-1} mode indicates the stretching mode associated with the short vanadyl (V = O) bond, with some broad low intensity peaks showing V-O-V stretching vibrations between 300–750 cm^{-1}. ED of IO V_2O_5 on SS substrates results in high crystalline quality V_2O_5 at 1.0 V, and ED at 4.0 V on heated SS is required over the same time period to replicate this crystalline quality within the IO structure. All IO's electrodeposited on the rougher FTO surface exhibited less defined Raman modes. On conductive SS, where the mass transport of VO^{2+} cations is driven at a lower voltage, the resulting crystallized V_2O_5 is of high crystal quality, and bending and stretching modes within the *xy* plane of the layered crystal structure characteristics of V_2O_5 become convoluted after ED at higher voltages. The opposite is observed in the same voltage range for ED on heated steel, where field breakdown of the oxide or conduction through point defects likely occurs to ensure that the measured current (reaction rate) facilitates ED of the V_2O_5 IO on the oxidized SS. At 4.0 V of heated SS, a high quality IO of V_2O_5 is formed after removal of the template.

XRD patterns were also obtained for the ED V_2O_5 IOs on FTO and SS seen in Fig. 10, with the corresponding reference patterns included. The reference peaks were also marked for each case, with the SS reference pattern not included as it only has peaks after 43 degrees. In each substrate, the (001) peak at 2θ∼20.37° is evident and confirmed the material has orthorhombic V_2O_5 with space group P*mmn*. In Fig. 10a there was also a sharp peak at 2θ∼37.6° that corresponds to the (200) tetragonal reflection. For an equivalent probe area, the relative intensities of reflections increases with the voltage of ED, closely following the mass increase measured and also estimated in Fig. 3

Downloaded on 2017-01-30 to IP 143.239.102.113 address. Redistribution subject to ECS terms of use (see ecsdl.org/site/terms_use) unless CC License in place (see abstract).

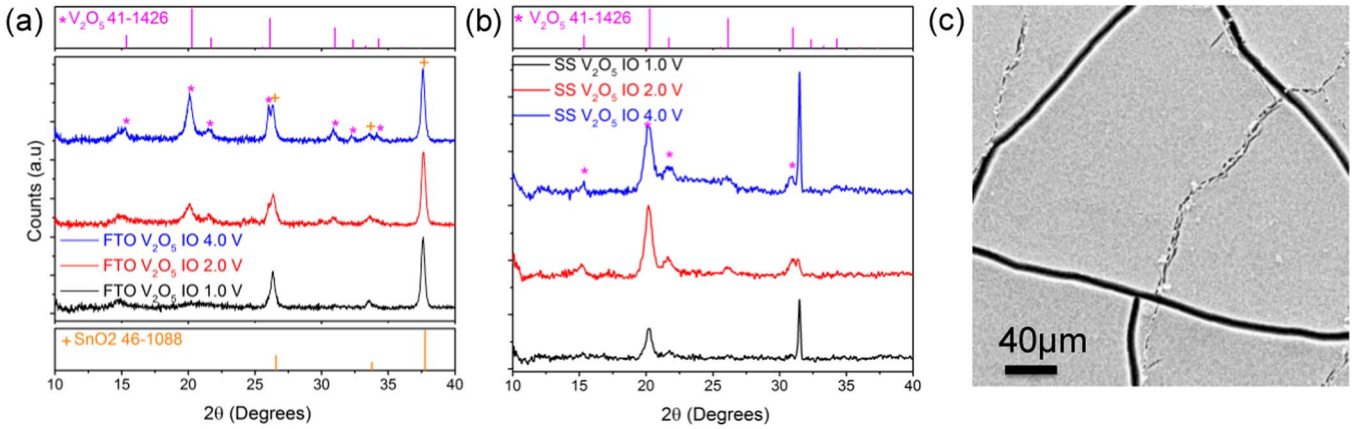


Figure 10. XRD spectra for the V_2O_5 IO ED at 1.0 V, 2.0 V, 4.0 V on FTO (a) and on SS (b) compared with the orthorhombic V_2O_5 reference spectrum (line graph) in each case, and the SnO_2 reference spectrum in (a). SS spectrum not included as there are no peaks before 40 degrees. (c) SEM image of large area electrodeposited V_2O_5 IO after thermal annealing.

by the Coulombic efficiency. Thus, the crystallinity is high quality at all voltages, with reflection intensity a function of the increased mass per unit volume in the porous material probed by the X-ray flux. The IO electrodeposited onto FTO also show an identical crystalline phase, with some extra reflections at higher angles apparent – note, IO electrodeposition onto FTO substrates is characteristically more robust and exhibits a greater adhesion. In drop-cast or dip-coated opal templates, the resulting IO only develops crystallinity during annealing to remove the spheres, otherwise the hydrolyzed liquid precursors form amorphous V_2O_5 IO.[7] Using electrodeposition in general results in a polycrystalline material prior to heating, and the crystallinity is annealed during thermal treatment to remove the opal template.

Conclusions

This work demonstrated the growth of vanadium oxide inverse opals and binary inverse opal structures by electrodeposition on transparent conducting FTO substrates and on stainless steel with and without a thermal oxide coating. Analysis of the potentiostatic growth profiles showed that IO growth in single and binary opal templates is diffusion limited and the early onset of current in the $I(t)$ profile is indicative of the substrate type. Heating SS forms an oxide coating that forces the initial ED current to increase to a steady state to overcome the resistive oxide, allowing IO to electrodeposit at relatively constant rate. After an initially high current on FTO and SS (without the resistive oxide), the current decreases via diffusion limited process also to a steady state IO growth mode. The diffusion constant and ionic diffusional tortuosity are negligible on FTO and SS at low voltages and marginal at 4.0 V, but tortuosity is significantly increased when large sphere diameter templates are used, and especially pronounced when binary opal templates are used, because of interstitial void filling by small spheres in binary opal templates. After analysis of the actual real surface area available at the surface, we propose that a reduction in this area contributes to tortuosity calculation (as it is defined as a ratio of D values for a similar packing factor) and IO growth mode in addition to the nature of the opal template. Raman scattering and X-ray diffraction confirm phase pure, high crystalline quality V_2O_5 is generally formed in all cases (voltages and substrates).

The electrodeposition of inverse opals and the influence of the template, voltage and substrate type are important for their applications in electrochemical technologies such as batteries, supercapacitors, electrochromics, photocatalysis and water splitting, to name a few. In all cases, the deposition should ensure intimate contact with the substrate, and ED ensures electrical interconnection within the 3D structured material. In addition, control over the macroporosity is important for ionic diffusional access to the surface for electrochromic and capacitive effects, and for Li-ion batteries.

Acknowledgments

This work was also supported by Science Foundation Ireland (SFI) through an SFI Technology Innovation and Development Award under contract no. 13/TIDA/E2761. This publication has also emanated from research supported in part by a research grant from SFI under grant Number 14/IA/2581.

References

1. L. S. Kibis, A. I. Stadnichenko, S. V. Koscheev, V. I. Zaikovskii, and A. I. Boronin, *J. Phys. Chem. C*, **116**, 19342 (2012).
2. M. Osiak, H. Geaney, E. Armstrong, and C. O'Dwyer, *J. Mater. Chem. A*, **2**, 9433 (2014).
3. G. Collins, E. Armstrong, D. McNulty, S. O'Hanlon, H. Geaney, and C. O'Dwyer, *Sci. Technol. Adv. Mater.*, **17**, 563 (2016).
4. P. Yang, T. Deng, D. Zhao, P. Feng, D. Pine, B. F. Chmelka, G. M. Whitesides, and G. D. Stucky, *Science*, **282**, 2244 (1998).
5. P. V. Braun and P. Wiltzius, *Nature*, **402**, 603 (1999).
6. S. C. Cassagneau and F. , *Adv. Mater.*, 34 (2002).
7. E. Armstrong, M. Osiak, H. Geaney, C. Glynn, and C. O'Dwyer, *CrystEngComm*, **16**, 10804 (2014).
8. S. John, *Phys. Rev. Lett.*, **58**, 2486 (1987).
9. E. Yablonovitch, *Phys. Rev. Lett.*, **58**, 2059 (1987).
10. J. D. Joannopoulos, P. R. Villeneuve, and S. H. Fan, *Nature*, **386**, 830 (1997).
11. G. A. Ozin, A. C. Arsenault, and L. Cademartiri, *Nanochemistry: A Chemical Approach to Nanomaterials*, Royal Society of Chemistry (2009).
12. A. Stein, B. E. Wilson, and S. G. Rudisill, *Chem. Soc. Rev*, **42**, 2763 (2013).
13. E. Armstrong and C. O'Dwyer, *J. Mater. Chem. C*, **3**, 6109 (2015).
14. J. Liu, Q. Zheng, M. D. Goodman, H. Zhu, J. Kim, N. A. Krueger, H. Ning, X. Huang, J. Liu, M. Terrones, and P. V. Braun, *Adv. Mater.*, **28**, 7696 (2016).
15. Y. Xia and B. Lim, *Nature*, **467**, 923 (2010).
16. S. J. Yeo, H. Kang, Y. H. Kim, S. Han, and P. J. Yoo, *ACS Appl. Mater. Interfaces*, **4**, 2107 (2012).
17. M. Kuwabara, *Photonic Crystals Fabricated by Sol–Gel Process*, p. 1, Springer International Publishing, Cham (2016).
18. Y. Zhao, X. Li, J. Liu, C. Wang, Y. Zhao, and G. Yue, *ACS Appl. Mater. Interfaces*, **8**, 6472 (2016).
19. F. Zhang, Y. Tang, H. Liu, H. Ji, C. Jiang, J. Zhang, X. Zhang, and C.-S. Lee, *ACS Appl. Mater. Interfaces*, **8**, 4691 (2016).
20. L. Chen, Y. Liang, H. Liu, W. Mai, Z. Lin, H. Xu, R. Fu, and D. Wu, *RSC Adv.*, **6**, 49661 (2016).
21. F. Li, M. Zeng, J. Li, X. Tong, and H. Xu, *RSC Adv.*, **6**, 26902 (2016).
22. D. R. Rolison, J. W. Long, J. C. Lytle, A. E. Fischer, C. P. Rhodes, T. M. McEvoy, M. E. Bourg, and A. M. Lubers, *Chem. Soc. Rev*, **38**, 226 (2009).
23. C. O'Dwyer, *Adv. Mater.* **28**, 5681 (2016).
24. O.-H. Kim, Y.-H. Cho, S. H. Kang, H.-Y. Park, M. Kim, J. W. Lim, D. Y. Chung, M. J. Lee, H. Choe, and Y.-E. Sung, *Nat. Commun.*, **4**, 2473 (2013).
25. E. Armstrong, M. O'Sullivan, J. O'Connell, J. D. Holmes, and C. O'Dwyer, *J. Electrochem. Soc*, **162**, D605 (2015).
26. X. Wang, P.-P. Sun, J. Qin, J. Wang, Y. Xiao, and M. Cao, *Nanoscale*, **8**, 10330 (2016).
27. H. Zhang, X. Yu, and P. V. Braun, *Nat. Nanotechnol.*, **6**, 277 (2011).

Downloaded on 2017-01-30 to IP 143.239.102.113 address. Redistribution subject to ECS terms of use (see ecsdl.org/site/terms_use) unless CC License in place (see abstract).

28. J. Luo, S. K. Karuturi, L. Liu, L. T. Su, A. I. Y. Tok, and H. J. Fan, *Sci. Rep.*, **2**, 451 (2012).
29. G. Yun, M. Balamurugan, H.-S. Kim, K.-S. Ahn, and S. H. Kang, *J. Phys. Chem. C*, **120**, 5906 (2016).
30. Z. Zhang, C. Ma, L. He, S. Zhu, X. Hao, W. Xie, W. Zhang, and Y. Zhang, *Nanoscale Res. Lett.*, **9**, 601 (2014).
31. Z. Tong, J. Hao, K. Zhang, J. Zhao, B.-L. Su, and Y. Li, *J. Mater. Chem. C*, **2**, 3651 (2014).
32. E. Armstrong, D. McNulty, H. Geaney, and C. O'Dwyer, *ACS Appl. Mater. Interfaces*, **7**, 27006 (2015).
33. D. McNulty, D. N. Buckley, and C. O'Dwyer, *J. Power Sources*, **267**, 831 (2014).
34. Y. Cao, D. Fang, R. Liu, M. Jiang, H. Zhang, G. Li, Z. Luo, X. Liu, J. Xu, W. Xu, and C. Xiong, *ACS Appl. Mater. Interfaces*, **7**, 27685 (2015).
35. J. M. Tarascon and M. Armand, *Nature*, **414**, 359 (2001).
36. J. Zhou, J. Qin, N. Zhao, C. Shi, E. Liu, F. He, J. Li, and C. He, *J. Mater. Chem. A*, **4**, 8734 (2016).
37. M.-S. Balogun, W. Qiu, J. Jian, Y. Huang, Y. Luo, H. Yang, C. Liang, X. Lu, and Y. Tong, *ACS Appl. Mater. Interfaces*, **7**, 23205 (2015).
38. D. McNulty, H. Geaney, E. Armstrong, and C. O'Dwyer, *J. Mater. Chem. A*, **4**, 4448 (2016).
39. K. A. Arpin, M. D. Losego, and P. V. Braun, *Chem. Mater.*, **23**, 4783 (2011).
40. M. P. B. Glazer, J. Cho, J. Almer, J. Okasinski, P. V. Braun, and D. C. Dunand, *Adv. Energy Mater.*, **5**, 1500466 (2015).
41. K. A. Arpin, M. D. Losego, A. N. Cloud, H. Ning, J. Mallek, N. P. Sergeant, L. Zhu, Z. Yu, B. Kalanyan, G. N. Parsons, G. S. Girolami, J. R. Abelson, S. Fan, and P. V. Braun, *Nat. Commun.*, **4** (2013).
42. H. Liu, H.-M. Cho, Y. S. Meng, and Q. Li, *ACS Appl. Mater. Interfaces*, **6**, 9842 (2014).
43. S. Kim, A. N. Mitropoulos, J. D. Spitzberg, H. Tao, D. L. Kaplan, and F. G. Omenetto, *Nat. Photon.*, **6**, 818 (2012).
44. D. Vernardou, D. Louloudakis, E. Spanakis, N. Katsarakis, and E. Koudoumas, *New J. Chem.*, **38**, 1959 (2014).
45. D. Rehnlund, M. Valvo, K. Edström, and L. Nyholm, *J. Electrochem. Soc*, **161**, D515 (2014).
46. J. Kim, H. S. Kim, J. H. Choi, H. Jeon, Y. Yoon, J. Liu, J.-G. Park, and P. V. Braun, *Chem. Mater*, **26**, 7051 (2014).
47. Z. Tong, H. Xu, G. Liu, J. Zhao, and Y. Li, *Electrochem. Commun*, **69**, 46 (2016).
48. Z. Tong, H. Yang, L. Na, H. Qu, X. Zhang, J. Zhao, and Y. Li, *J. Mater. Chem. C*, **3**, 3159 (2015).
49. F. G. Cottrell, *Z. Phys. Chem.*, **42**, 385 (1903).
50. D. Grujicic and B. Pesic, *Electrochim. Acta*, **47**, 2901 (2002).
51. S. Ramírez-García, S. Alegret, F. Céspedes, and R. J. Forster, *Analyst*, **127**, 1512 (2002).
52. E. Armstrong, W. Khunsin, M. Osiak, M. Blömker, C. M. S. Torres, and C. O'Dwyer, *Small*, **10**, 1895 (2014).
53. J. V. Sanders and M. J. Murray, *Nature*, **275**, 201 (1978).
54. C. J. Kiely, J. Fink, M. Brust, D. Bethell, and D. J. Schiffrin, *Nature*, **396**, 444 (1998).
55. K. P. Velikov, C. G. Christova, R. P. A. Dullens, and A. van Blaaderen, *Science*, **296**, 106 (2002).
56. J. V. Sanders, *Nature*, **204**, 1151 (1964).
57. E. L. Cussler, *Diffusion*, Cambridge University Press: New York (1997).
58. J. C. Maxwell, *Treatise on Electrochemistry and Magnetism*, Oxford University Press (1892).
59. J. Crank, *The Mathematics of Diffusion*: 2d Ed, Oxford University, Press: New York (1975).
60. E. A. Mason and A. P. Malinauskas, *Gas Transport in Porous Media: The Dusty-Gas Model*, Elsevier: Amsterdam (1983).
61. M. R. Newton, K. A. Morey, Y. Zhang, R. J. Snow, M. Diwekar, J. Shi, and H. S. White, *Nano Lett.*, **4**, 875 (2004).
62. C. Kittel and D. F. Holcomb, *Introduction to Solid State Physics*, p. 547 (1967).
63. R. Baddour-Hadjean, A. Marzouk, and J. P. Pereira-Ramos, *J. Raman Spectrosc* **43**, 153 (2012).
64. R. Baddour-Hadjean, J. P. Pereira-Ramos, C. Navone, and M. Smirnov, *Chem. Mater.*, **20**, 1916 (2008).
65. C. Bhandari and W. R. Lambrecht, *Phys. Rev. B*, **89**, 045109 (2014).
66. R. Baddour-Hadjean, J. Pereira-Ramos, C. Navone, and M. Smirnov, *Chem. Mater*, **20**, 1916 (2008).
67. R. Baddour-Hadjean and J.-P. Pereira-Ramos, *Chem. Rev*, **110**, 1278 (2009).
68. C. O'Dwyer, V. Lavayen, S. Newcomb, M. A. Santa Ana, E. Benavente, G. Gonzalez, and C. S. Torres, *J. Electrochem. Soc*, **154**, K29 (2007).

Downloaded on 2017-01-30 to IP **143.239.102.113** address. Redistribution subject to ECS terms of use (see **ecsdl.org/site/terms_use**) unless CC License in place (see abstract).